2D $Ge_2Se_2P_4$ Monolayer
A Versatile Photocatalyst for Sustainable Water Splitting

Vu, Tuan V.; Hieu, Nguyen N.; Vo, Dat D.; Kartamyshev, A. I.; Tong, Hien D.; Trinh, Thuat T.; Khuong Dien, Vo; Haman, Zakaryae; Dey, Poulumi; Khossossi, Nabil

DOI
10.1021/acs.jpcc.3c07237

Publication date
2024

Document Version
Final published version

Published in
Journal of Physical Chemistry C

THE JOURNAL OF PHYSICAL CHEMISTRY C
A JOURNAL OF THE AMERICAN CHEMICAL SOCIETY

pubs.acs.org/JPCC

Article

2D $Ge_2Se_2P_4$ Monolayer: A Versatile Photocatalyst for Sustainable Water Splitting

Tuan V. Vu,* Nguyen N. Hieu, Dat D. Vo, A. I. Kartamyshev, Hien D. Tong, Thuat T. Trinh, Vo Khuong Dien, Zakaryae Haman, Poulumi Dey,* and Nabil Khossossi*

Cite This: *J. Phys. Chem. C* 2024, 128, 4245−4257

Read Online

ACCESS | Metrics & More | Article Recommendations

ABSTRACT: This study aims to identify photo-/electrocatalysts that can enhance the oxygen evolution reaction (OER), hydrogen evolution reaction (HER), and oxygen reduction reaction (ORR), which are of utmost importance in electro-/photochemical energy systems, such as solar energy, fuel cells, water electrolyzers, or metal-air batteries. Our study focused on investigating the 2D $Ge_2Se_2P_4$ monolayer and found that it exhibits a bifunctional photocatalyst with a very high solar-to-hydrogen efficiency. The two-dimensional (2D) $Ge_2Se_2P_4$ monolayer has superior HER activity compared to that of most 2D materials, and it also outperforms the reference catalysts $IrO_2(110)$ and Pt(111) in terms of low overpotential values for ORR and OER mechanisms. Such superior catalytic performance in the 2D $Ge_2Se_2P_4$ monolayer can be attributed to its electron states, charge transfer process, and suitable band alignments referring to normal hydrogen electrodes. Overall, the study suggests that the $Ge_2Se_2P_4$ monolayer could be an excellent bifunctional catalyst for advancing photo-/electrochemical energy systems.

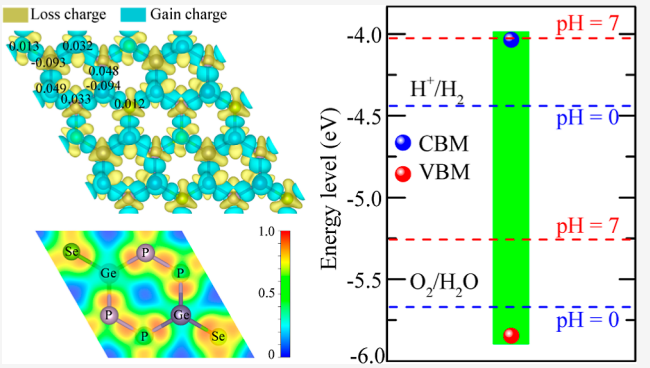

INTRODUCTION

The overuse of fossil fuel energy sources has worsened energy depletion, environmental damage, and global warming. This builds up the pressure on searching for renewable energies, with hydrogen energy emerging as one of the most auspicious renewable energy resources. Hydrogen fuel cells have large capacity and fast refueling time, and they only emit water vapor when generating electricity.[1,2] Nevertheless, the majority of hydrogen is presently generated via costly methods such as electrolysis and steam reforming, which still rely on fossil fuels. Therefore, the utilization of solar energy for the production of hydrogen is widely recognized as having significant potential.[3−5] Two-dimensional (2D) nanostructures are ideal for this purpose because they have a high surface-to-volume ratio, short charge transport distances, and other beneficial features that vary depending on the material family.[6−8] The ZnSe monolayer, for example, was reported to have a high photocurrent density of up to 2.14 mA cm^{-2}.[9] Meanwhile, group-III and group-IV monochalcogenides, germanium, and carbon nitrides are monolayers with a high visible light absorption rate.[10−14] Transition-metal dichalcogenides are good 2D photocatalytic materials with high charge carrier mobility.[15−17] 2D materials have many extraordinary physical properties with many promising applications in next-generation devices.[18−20]

Recently, triphosphide monolayers XP_3 [X = Sn, Ge, Ca, and In] have been intensively investigated due to the diversity of their components and unique photocatalytic properties.[21−26] Since 1970, 3D SnP_3 has been experimentally reported.[27] Furthermore, theoretical calculations have predicted that SnP_3 can exist in a monolayer form.[28] The novel SnP_3 monolayer is expected to have high carrier mobility and a good optical absorption rate that is beneficial for photovoltaic applications.[23,29] Recently, the monolayer GeP_3 was shown to have a charge carrier mobility of some 10^3 cm^2 V^{-1} s^{-1}; this characteristic is also observed in GaP_3, InP_3, SnP_3, and TlP_5.[25,28,30,31] Jing and co-workers recently suggested the 2D honeycomb-layered structure of GeP_3 with high carrier mobility (8.84×10^3 cm^2 V^{-1} s^{-1}) for the bilayer.[21] Many metal phosphide structures, including SnP_3, InP_3, and TlP_5, have been theoretically investigated. The metal phosphide structures were found to have high carrier mobility, which makes them suitable for applications in optoelectronic

Received: October 31, 2023
Revised: February 6, 2024
Accepted: February 19, 2024
Published: February 29, 2024

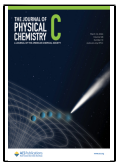

applications.[25,28,30,31] Unfortunately, the bandgap of these structures is found to be small, from 0.55 to 1.15 eV, implying that they are unsuitable for photocatalytic water splitting. Therefore, their electronic structures must be engineered to match the requirement of redox processes to generate hydrogen using water and solar energy. The existing studies show that the desired electronic structure of 2D layered nanostructures can be obtained by substituting the appropriate element for one of the host atoms.[32−34] Recently, $Sn_2S_2P_4$ has been found to be semiconducting with a wider bandgap (1.77 eV)[35] than that of SnP_3 (0.83 eV).[23] The bandgap and band-edges of $Sn_2S_2P_4$ are appropriate for applications in water splitting technologies. Besides, 2D ternary structures $Ge_2P_4S_2$, $Ge_2As_4S_2$,[36] and $BiMP_6$,[37] have been shown to possess advantageous properties for photocatalytic processes.

In this study, the $Ge_2Se_2P_4$ monolayer was constructed by substituting Se for P in the GeP_3 monolayer. The ability of the $Ge_2Se_2P_4$ monolayer to serve as a photocatalyst in redox reactions is studied based on the examination of its electronic, optical, charge transfer, and related characteristics. It is worth noticing that the transition of a compound from bulk to 2D phase reduces the screening of the electric field in materials; therefore, the Coulomb interaction increases, and the electron−hole pairs (excitons) become more strongly bonded.[38] As a result, excitons have a substantial impact on the interaction of 2D materials with incident photons, as well as their optical properties.[39−42] Therefore, the exciton effect was also considered when determining the optical features of the $Ge_2Se_2P_4$ material.

COMPUTATIONAL METHOD

The first-principles study in this work was performed by the Vienna ab initio simulation package.[43,44] In the projector augmented wave method,[45] the electron−core interaction is replaced by a pseudopotential, whose wave function is expanded with a cutoff energy of 500 eV. The exchange−correlation of valence electrons is treated by the GGA-PBE method (generalized gradient approximation which is parameterized by Perdew, Burke, and Ernzerhof)[46] and hybrid functional Heyd−Scuseria−Ernzerhof (HSE06).[47] The spin−orbit coupling (SOC) was included in the calculations for self-consistency to investigate the influence of the SOC on the electronic features of the studied structure.[48] The quasiparticle energy spectra were evaluated using the single-shot GW (G_0W_0) approximation[49] on the exchange−correlation self-energies, with the screening effect included using the Hybertsen−Louie plasmon-mode model.[50] In the layered $Ge_2Se_2P_4$ structure, the van der Waals interactions may exist; therefore, these interactions were also taken into account by applying the DFT-D3 approach, which was developed by Grimme.[51] The Brillouin zone is constructed with a 20 × 20 × 1 *k*-point mesh in the Γ sampling technique. The atomic model of $Ge_2Se_2P_4$ was constructed based on 2D GeP_3,[21] where Se atoms were substituted for P atoms. The height of the unit cell was set to be 25 Å to reduce interactions between periodic slabs. The structural optimization reaches convergence as the difference in total energy and the forces acting on atoms are smaller, respectively, than 10^{-5} eV and 0.001 eV/Å. The mechanical stability of the $Ge_2Se_2P_4$ monolayer was estimated based on its phonon dispersion, which was carried out using the PHONOPY code,[52] where the density functional perturbation theory[53] was applied for a 4 × 4 × 1 supercell. The thermal stability was studied by performing ab initio molecular dynamics (AIMD) simulations.[54] The transport features were examined by applying the deformation potential (DP) theory.[55] To incorporate excitonic effects in optical characteristics, we solved the Bethe−Salpeter equation (BSE)[56] of the interacting two-particle Green's function. The Tamm−Dancoff approximation[57] was used, and energy cutoff and *k*-point sampling were set to resemble those in the G_0W_0 calculations. A Lorentzian function with a maximum broadening of 50 meV was employed as a substitute for the delta function. In this study, the excitonic effects were treated by using the three lowest conduction bands and the four highest valence bands in the Bethe−Salpeter kernel.

RESULTS AND DISCUSSION

Stability and Mechanical Features of the $Ge_2Se_2P_4$ Monolayer. The $Ge_2Se_2P_4$ monolayer was constructed using the buckling hexagonal structure of GeP_3,[58] which remained almost unchanged after structural optimization. The equilibrium structure of a $Ge_2Se_2P_4$ monolayer is depicted in Figure 1, and its lattice parameter *a* is 6.95 Å, which is very close to

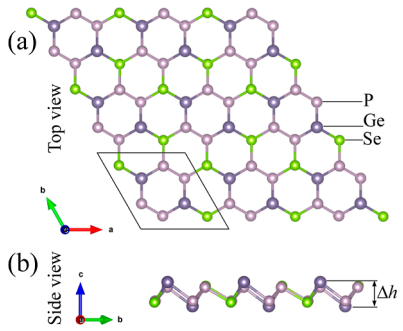

Figure 1. Optimized atomic structure of the $Ge_2Se_2P_4$ monolayer with the hexagonal cell shown in (a) top view and (b) side view. The rhombus in (a) represents the unit cell.

that of a 2D GeP_3 monolayer. However, the thickness h of the monolayer decreases significantly from 2.42 Å of 2D GeP_3 to 1.90 Å of the $Ge_2Se_2P_4$ monolayer.[58] This decrease has also been observed in $Ge_2S_2P_4$, $Ge_2As_2P_4$, and $Sn_2S_2P_4$ monolayers, whose thickness is 1.85−1.91 Å.[35,36] These results allow an assumption that when phosphorus atoms in the 2D GeP_3 are replaced by atoms with more electrons to form ternary compounds $Ge_2X_2P_4$ (X = S, Se, and As), there are more electrons to occupy the hybridized sp^2 orbitals. Because of this, the in-plane σ-bonds (formed by the end-to-end overlap of hybridized sp^2 orbitals) become stronger in keeping the monolayer flat; meanwhile, the out-of-plane π-bonds (formed by the side-by-side overlap of unhybridized pz orbitals) are weakened, causing less buckling effect.

The cohesive energy of the $Ge_2Se_2P_4$ monolayer is calculated to be −4.67 eV; therefore, it is energetically stable. Some monolayers such as GeS, GeSe, and SeTe have been successfully synthesized.[59−61] The cohesive energy of these compounds is even less negative than that of the $Ge_2Se_2P_4$ monolayer, indicating the possible experimental syntheses of $Ge_2Se_2P_4$ nanosheets. To further investigate the stability of $Ge_2Se_2P_4$, we calculate the phonon dispersions of $Ge_2Se_2P_4$. The $Ge_2Se_2P_4$ monolayer has a buckling hexagonal structure, so its phonon dispersion, presented in Figure 2a, was plotted along the Γ−*M*−*K*−Γ path. The dynamical stability of $Ge_2Se_2P_4$ is confirmed by its phonon spectrum, as shown in

https://doi.org/10.1021/acs.jpcc.3c07237
J. Phys. Chem. C 2024, 128, 4245−4257

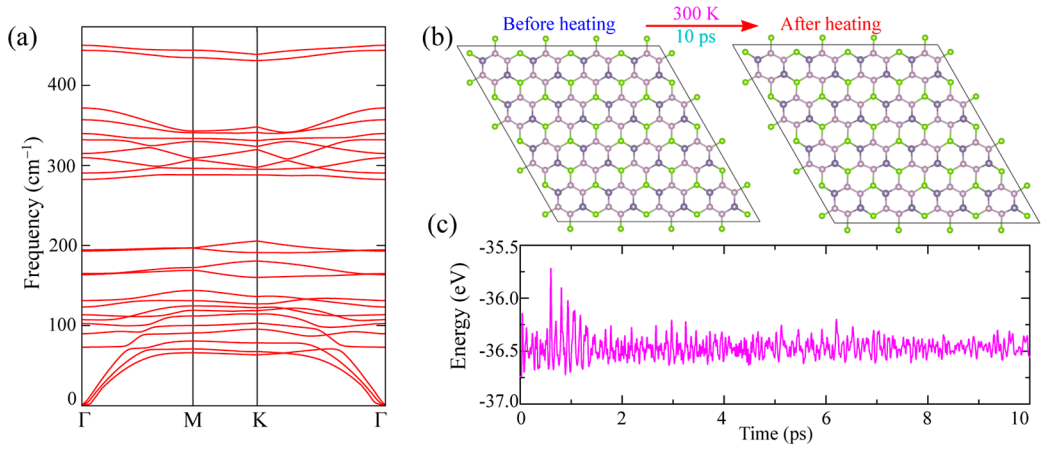

Figure 2. Energetical features of the $Ge_2Se_2P_4$ monolayer: (a) phonon dispersion, (b) atomic structure before and after heating, and (c) time-dependent total energy.

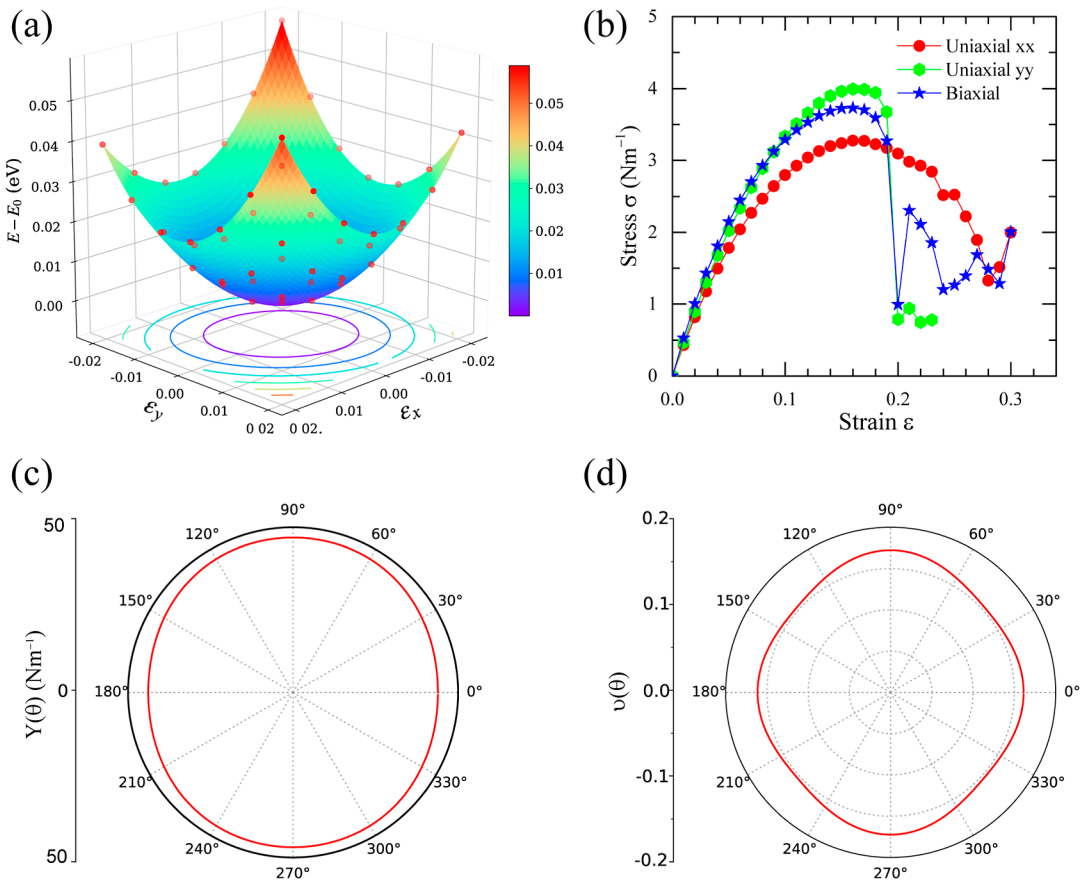

Figure 3. Elastic properties of the $Ge_2Se_2P_4$ monolayer: (a) 3D presentation of strain energy versus strain and (b) stress versus strain. In-plane angle (θ)-dependent Young's modulus $Y(\theta)$ (c) and Poisson's ratio $\upsilon(\theta)$ (d) of $Ge_2Se_2P_4$.

Figure 2a. It is noted that small negative frequencies are present around the Γ point, which may be related to in-plane bending.[62] These small negative frequencies can be reduced by applying strain.[63] The thermal stability of $Ge_2Se_2P_4$ was tested by the AIMD simulation at 300 K within 10 ps. From Figure 2b, we can see that the atomic structure of $Ge_2Se_2P_4$ stays almost the same after being heated at 300 K. After 2 ps of heating, the energy variation quickly decreases, and the total energy remains near 36.5 eV, indicating the thermal stability at room temperature of the $Ge_2Se_2P_4$ monolayer, as depicted in Figure 2c.

Elastic features are also important in determining the possible syntheses of the $Ge_2Se_2P_4$ monolayer as well as its practical uses. As shown in Figure 3a, the $Ge_2Se_2P_4$ monolayer responds well to uniaxial and biaxial strains. The strains (ε from −2 to 2%) along the x and y axes cause the energy of the system to increase significantly. The energy is lowest at zero strain; therefore, the optimized structure is the most energetically stable one. Meanwhile, the stress rapidly increases as the rate of strain gets higher, as shown in Figure 3b, especially the uniaxial strain along the y-direction. It is worthy to notice that strains of 18−20% cause the highest stress. A

https://doi.org/10.1021/acs.jpcc.3c07237
J. Phys. Chem. C 2024, 128, 4245−4257

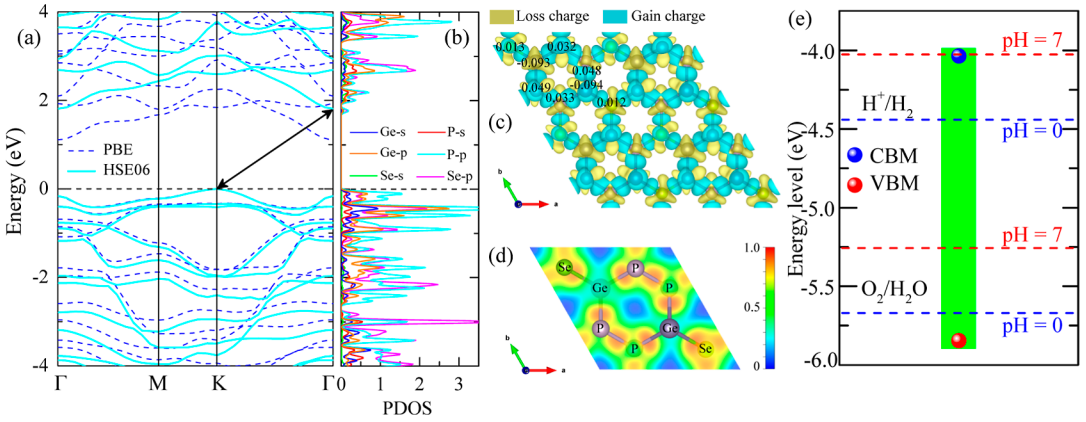

Figure 4. (a) Band structure, (b) partial density of state, (c) Bader charge and difference in electron density, (d) electron localization function, and (e) band edge alignment of the $Ge_2Se_2P_4$ monolayer.

further increase of strain results in a sharp drop in stress, and the stress−strain relationship is not continuous. This result indicates that the ideal strain is 18−20%, and strains higher than 20% can cause structural failure in the $Ge_2Se_2P_4$ monolayer. The uniaxial strain along the *x*-axis causes a maximum stress of 3.4 N m^{-1}, while biaxial strains cause a maximum stress of 3.8 N m^{-1}. Also, the strain along the *y*-direction causes the largest stress of more than 4.2 N m^{-1}. Among the three types of strains, the uniaxial strain along the *x*-direction is well resisted by the $Ge_2Se_2P_4$ monolayer because the stress of the system slowly decreases as the strains are higher than 20%. However, this decrease is slow, indicating that the elasticity of the system slowly vanishes.

In the case of hexagonal monolayers, it is important to determine the C_{11}, C_{22}, C_{12}, and C_{66} elastic constants based on which the 2D Young's modulus $Y(\theta)$ and Poisson's ratio $\upsilon(\theta)$ can be derived for each value of in-plane angle θ.[64] The obtained results for $Y(\theta)$ and $\upsilon(\theta)$ are depicted in Figure 3c,d as nearly circles, implying that these two elastic parameters are almost independent of the direction. The calculated C_{11}, C_{22}, C_{12}, and C_{66} are 45.14, 7.78, 48.23, and 19.94 N m^{-1}, respectively. These elastic constants satisfy the conditions $C_{11} > |C_{12}|$, $C_{11}C_{12}-C_{12}^2 > 0$, and $C_{66} > 0$ of Born−Huang's stability criteria,[65] indicating the stability of $Ge_2Se_2P_4$ under pressures. The Poisson's ratios along the *x*- and *y*-axes are 0.16 and 0.17, which are close to those of graphene,[66] a well-known high-strength material. Similar to $Ge_2S_2P_4$ and $Ge_2As_2P_4$ monolayers,[36] Young's modulus of the $Ge_2Se_2P_4$ monolayer (43.89−46.89 N m^{-1}) is rather small in comparison with that of graphene, which is about 342 N m^{-1}.[67]

Electronic Properties of the $Ge_2Se_2P_4$ Monolayer. The stability of the $Ge_2Se_2P_4$ monolayer is studied and confirmed based on its energetic and mechanical properties. To explore other properties of this newly proposed monolayer, it is necessary to understand its electronic structure. Generally, the GGA-PBE method can provide a reliable electronic structure with a low computational cost. However, the exchange−correlation is not treated well, resulting in an unphysical phenomenon when an electron repulses itself. This gives rise to the energy levels of the valence bands, while the unoccupied conduction bands stay the same, and the band gap becomes smaller than it should be.[68] Therefore, a correction must be introduced to the exchange−correlation, and this is done in the hybrid functional called HSE06.[69] The two methods were applied to calculate the band structure (along the Γ−*M*−*K*−Γ path) of the $Ge_2Se_2P_4$ monolayer. In Figure 4a, the bands obtained using the GGA-PBE method are presented with blue dashed curves, and the solid blue bands were examined with the HSE06 method. The band diagrams of $Ge_2Se_2P_4$ examined by the two methods are similar to the conduction band minimum (CBM) at the Γ point and the valence band maximum (VBM) at the *K* point. Therefore, the calculation shows that the $Ge_2Se_2P_4$ monolayer is a semiconductor with an indirect band gap. The bandgap calculated with the GGA−PBE method is 1.11 eV, while the bandgap obtained by applying the HSE06 method is 1.81 eV. The HSE06 bandgap of $Ge_2Se_2P_4$ is very close to that of $Ge_2S_2P_4$ and $Sn_2S_2P_4$ monolayers.[35,36]

The bandgaps of $Ge_2Se_2P_4$, $Ge_2S_2P_4$, and $Sn_2S_2P_4$ are about 1 eV larger than those of 2D GeP_3 and SnP_3, which are 0.55−0.72 eV.[21,28,58] As revealed in Figure 4b, the band diagram of $Ge_2Se_2P_4$ is mainly constructed by sp^2 hybridization. Any change to these hybridized orbitals can cause significant variation in the electronic features of the $Ge_2Se_2P_4$ material. It is obvious that the S and Se elements have more electrons than the P element does. When one of these elements substitutes for a P atom in GeP_3 or SnP_3, there are more electrons to occupy the valence bands leading to degeneracy and orbital splitting which widens the band gap. The role of orbitals from each constituent element is well demonstrated in Figure 5,

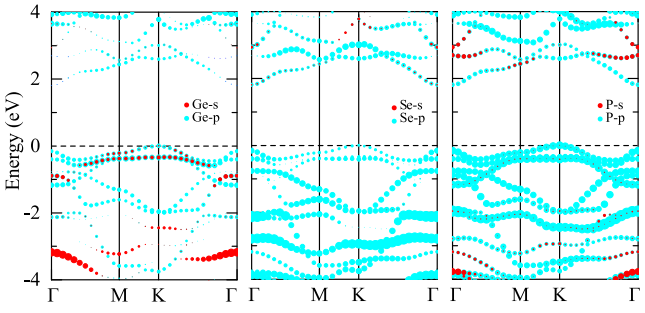

Figure 5. Weighted band structure of the $Ge_2Se_2P_4$ monolayer.

where s-orbitals from Se atoms donate a minor part in both the valence and conduction bands. Meanwhile, there are more s-orbitals from Ge atoms in the valence bands, and the s-orbitals predominate in the conduction bands. The p-orbitals from Se and P atoms play an important role in determining the band gap because they mainly construct the valence and conduction

https://doi.org/10.1021/acs.jpcc.3c07237
J. Phys. Chem. C 2024, 128, 4245−4257

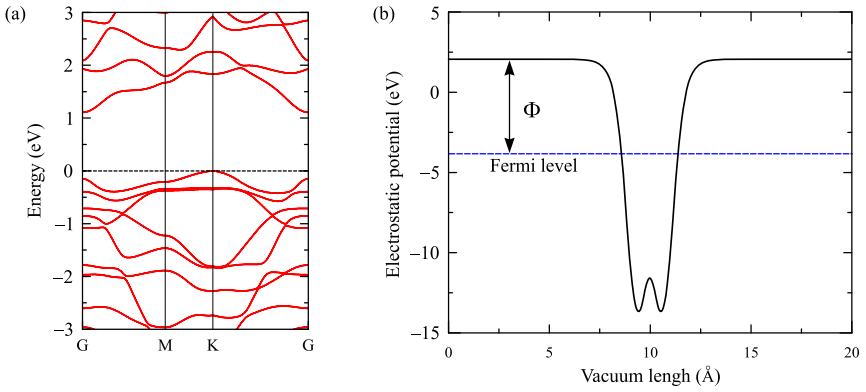

Figure 6. PBE + SOC band structure (a) and electrostatic potential (b) of the $Ge_2Se_2P_4$ monolayer.

bands. The electron localization function, demonstrated in Figure 4d, shows the covalent bonding nature of the $Ge_2Se_2P_4$ monolayer as there is high electron density in the areas between constituent atoms. Electrons mainly concentrate on the Se sites; the Bader charge distribution in Figure 4c shows a charge transfer of 0.093−0.094 |e| to Se ions.

Further, we examine the band diagram of $Ge_2Se_2P_4$ by the PBE + SOC method to consider the effect of the SOC on its electronic features. It is found that the effect of the SOC on the electronic properties of the $Ge_2Se_2P_4$ monolayer is insignificant. There is no significant change in the band structure of the $Ge_2Se_2P_4$ monolayer when SOC is included, as shown in Figure 6a. The PBE + SOC band gap of the $Ge_2Se_2P_4$ monolayer is found to be 1.10 eV, which is very close to its GGA−PBE bandgap (1.11 eV). In Figure 6b, we show the calculated results for the electrostatic potential of the $Ge_2Se_2P_4$ monolayer. Through the obtained electrostatic potential, we can find the work function based on the obtained Fermi and vacuum levels. The Fermi level is found at −3.77 eV, and the work function Φ of the $Ge_2Se_2P_4$ material is 5.85 eV.

The work of Fujishima and Honda in 1972[70] has stimulated great effort in searching for efficient photocatalysts for water splitting. Among many candidates, 2D materials are considered to be very promising materials as they have large surface areas, fast carrier mobilities, and light harvesting ability.[71,72] All the 2D materials must have appropriate band-edge positions, where the CBM exhibits a greater positive value compared to that of the reduction potential and the VBM has a greater negativity value compared to that of the oxidation potential.[73,74] The possibility of the $Ge_2Se_2P_4$ monolayer to work as a photocatalyst in water splitting applications can be determined based on the positions of CBM and VBM relative to the redox potential, as presented in Figure 4e; the CBM exceeds the reduction potential, while the VBM is lower than the oxidation potential. Therefore, the $Ge_2Se_2P_4$ monolayer can trigger both hydrogen and oxygen production from water using sunlight.

Optical and Transport Properties of the $Ge_2Se_2P_4$ Monolayer. Besides electronic properties, the $Ge_2Se_2P_4$ monolayer may possess interesting optical properties that could be useful in optoelectronic applications. The optical properties could be comprehended through the dielectric functions, which are represented by $\varepsilon(\omega) = \varepsilon_1(\omega) + i\varepsilon_2(\omega)$. In which, the imaginary part of dielectric functions is related to the excitation of electrons from the occupied states $|vk\rangle$ to the unoccupied ones $|ck\rangle$ and can be achieved through Fermi's golden rule[75]

$$\varepsilon_2(\omega) \propto \sum_{vck} |\langle vk|\hat{e}\cdot p|ck\rangle|^2 \delta(\omega - E_{ck} - E_{vk}) \quad (1)$$

where the oscillation strength and the transition energy of the absorbance spectrum, correspondingly, are directly related to the square of the velocity matrix element $|\langle vk|\hat{e}\cdot p|ck\rangle|^2$ and the electronic joint density of states $\delta(\omega - E_{ck} - E_{vk})$. The real part $\varepsilon_1(\omega)$ is then obtained via the Kramers−Kronig relations.[76]

The dielectric functions that include and exclude electron−hole interactions are shown by the blue (G_0W_0-RPA) and the red (G_0W_0-BSE) curves in Figure 7a. The static dielectric

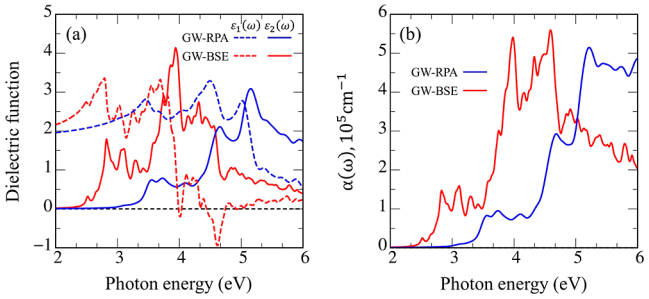

Figure 7. Calculated dielectric function (a) and absorption coefficient (b) of the $Ge_2Se_2P_4$ monolayer by the G_0W_0-RPA and G_0W_0-BSE methods.

constant $\varepsilon_1(0)$ of the $Ge_2Se_2P_4$ monolayer is approximately 2.0 (G_0W_0-RPA) and 2.2 (G_0W_0-BSE), consistent with its large electronic band gap nature.[77] Concerning the imaginary part $\varepsilon_2(\omega)$, optical gaps of approximately 3.02 eV (G_0W_0-RPA) and 2.41 eV (G_0W_0-BSE) are obtained. The significant red shift in the optical gap and the strong modification of the $\varepsilon_2(\omega)$ spectra of G_0W_0-BSE to that of G_0W_0-RPA indicate the presence of strong excitonic effects due to quantum confinement and the absence of vertical electronic screening. The excitonic binding, which is determined by the difference in energy between the optical gaps in cases with and without the excitonic effect, is found to be 0.61 eV. This value of the excitonic binding is comparable to similar 2D materials, such as MoS_2 (0.96 eV)[78] and WS_2 (0.71 eV).[79]

In addition to the dielectric functions, the optical absorption spectra $\alpha(\omega)$ could provide more information on the optical characteristics of the $Ge_2Se_2P_4$ monolayer, which is important for practical applications. The absorbance spectra are rather weak within the visible region, with typical values $\alpha(\omega)$ of ≈1.0 × 10^5 cm^{-1} (G_0W_0-RPA) and ≈1.5 × 10^5 cm^{-1} (G_0W_0-BSE) for energies within the range of 2.0 eV < ω < 4.0 eV. However,

https://doi.org/10.1021/acs.jpcc.3c07237
J. Phys. Chem. C 2024, 128, 4245−4257

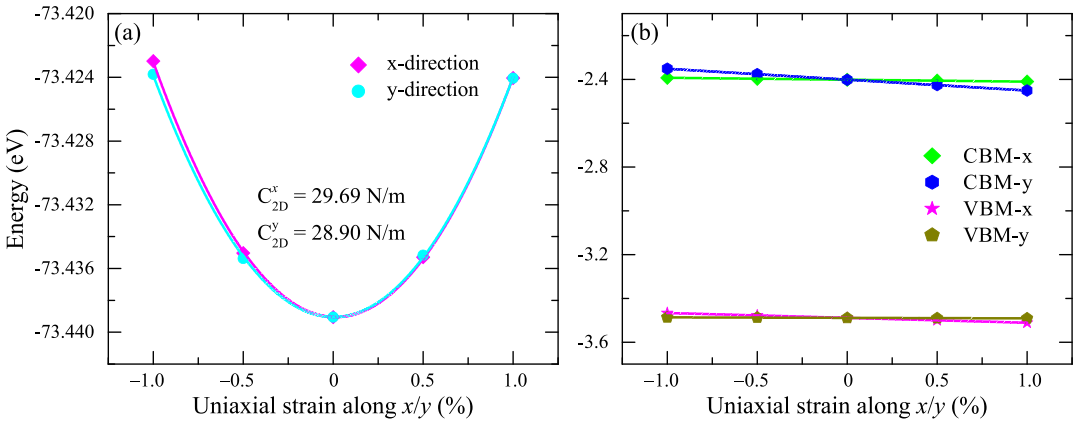

Figure 8. Total energy (a) and band-edge positions (b) as functions of uniaxial strains ϵ along the x and y directions of the $Ge_2Se_2P_4$ lattice.

the optical absorption intensity significantly increases after activation, particularly in the ultraviolet region (as illustrated in Figure 7b). This characteristic makes $Ge_2Se_2P_4$ useful for high-energy optoelectronic devices.

Charge carrier mobility is a critical attribute of prospective photocatalytic materials. For a 2D material, the charge carrier mobility is defined as $\mu_{2D} = \frac{e\hbar^3 C_{2D}}{k_B T m^* \bar{m} E_d^2}$. Here, e indicates the elementary charge, $\hbar$ is the Planck constant, and k_B refers to the Boltzmann constant. The 2D elastic constant $C_{2D} = (\partial^2 E(\varepsilon)/\partial\varepsilon^2)\Omega_0^{-1}$, where Ω_0 is the volume of the unit cell, and the total energy $E(\varepsilon)$ is a function of uniaxial strain ε, which is shown in Figure 7a. The effective mass $m^* = \hbar^2(\partial^2 E(k)/\partial^2 k)^{-1}$, where total energy $E(k)$ is a function of the k-vector in the reciprocal space. Finally, the deformation energy $E_d = \Delta E_{edge}/\varepsilon$, where the band edge alignment E_{edge} is a function of uniaxial strain ε, as presented in Figure 8b.

The obtained values for the carrier mobilities of $Ge_2Se_2P_4$ are revealed in Table 1. It is demonstrated that the mobilities

Table 1. Effective Mass m^*, Elastic Modulus C_{2D}, DP E_d, and Mobility of Carriers μ_{2D} of $Ge_2Se_2P_4$ along the x-/y-Direction[a]

carrier type	direction	C_{2D} (N m^{-1})	$m^*(m_0)$	E_d (eV)	μ_{2D} (cm^2 V^{-1} s^{-1})
electron	X	29.69	0.38	−0.88	7396.35
	Y	28.90	0.23	−4.98	375.35
hole	X	29.69	0.87	−2.23	155.95
	Y	28.90	1.01	−0.23	12275.86

[a] m_0 is the mass of a free electron.

of both the electron and hole are very high, signifying the good photocatalytic property of the $Ge_2Se_2P_4$ monolayer. Mobility also strongly depends on the examined direction and the carrier type. This is another advantage because the electron−hole separation in the $Ge_2Se_2P_4$ monolayer is expected to be enhanced. The electron mobility along the x-direction is 7396.35 cm^2 V^{-1} s^{-1}, while the hole mobility along the y-direction is 12,275.86 cm^2 V^{-1} s^{-1}. The obtained electron mobility of the $Ge_2Se_2P_4$ monolayer is higher than that of GeP_3 (700 cm^2 V^{-1} s^{-1}),[21] SnP_3 (5020 cm^2 V^{-1} s^{-1}),[23] and $Sn_2S_2P_4$ (1923.42 cm^2 V^{-1} s^{-1}).[35] Also, it is noted that the carrier mobility of $Ge_2Se_2P_4$ is higher than that of 2D GeP_3;[21] therefore, substitution is expected to be a good way to improve the transport properties of Ge-based 2D materials. With high charge carrier mobility, $Ge_2Se_2P_4$ is a competitive candidate for photocatalytic applications among other well-known 2D nanomaterials such as black phosphorus, MoS_2, and WS_2.[15,80]

Gibbs Free Energy Changes for the Hydrogen Evolution Reactions and Oxygen Evolution Reactions. To identify the most suitable catalyst for the hydrogen evolution reaction (HER), it is crucial to evaluate the adsorption energy of hydrogen atoms on the material surface. The adsorption energy, denoted as E_{H^*}, is related to the Gibbs free energy, ΔG_{H^*}, through the following equation

$$\Delta G_{H^*} = \Delta E_{H^*} + \Delta E_{ZPE} - T\Delta S + \Delta G_U - \Delta G_{pH} \quad (2)$$

where the hydrogen is adsorbed onto a particular surface location of a certain substance, ΔE_{H^*} denotes the adsorption energy computed for intermediate hydrogen adsorbed on the monolayer, as defined below

$$\Delta E_{H^*} = \left(E_{nH^*} - E_{(n-1)H^*} - \frac{1}{2}E_{H_2}\right) \quad (3)$$

where E_{nH^*} represents the energy with n hydrogen adsorbed on the monolayer, $E_{(n-1)H^*}$ stands for the free energy of the $(n-1)$ hydrogen coverage system, and E_{H_2} is the energy of the H_2 molecule in the gas phase. In eq 2, ΔE_{ZPE} denotes the difference in zero-point energy corrections and has been found to be 0.04 eV. The ΔS describes the difference in entropy and can be estimated as the entropy of H_2 gas under normal circumstances, as written as

$$\Delta S = \left(S_H - \frac{1}{2}S_{H_2}\right) \approx -\frac{1}{2}S^0_{H_2} \quad (4)$$

where $\frac{1}{2}S^0_{H_2}$ refers to the entropy of the H_2 molecule under the standard conditions and the value is 130 mol^{-1} K^{-1}.[81] In this context, the optimal value for HER is ΔG_{H^*} equal to zero. The theoretical overpotential η_{HER} for HER is defined as a function of ΔG_{H^*} as follows

$$\eta_{HER} = -\frac{|\Delta G_{H^*}|}{e} \quad (5)$$

The oxygen evolution reaction (OER) and oxygen reduction reaction (ORR) mechanisms proceed through a 4e$^-$ transferred reaction pathway as follows

$$H_2O(l) + {}^* \rightarrow OH^* + H^+ + e^- \quad (6)$$

$$OH^* \rightarrow O^* + H^+ + e^- \quad (7)$$

https://doi.org/10.1021/acs.jpcc.3c07237
J. Phys. Chem. C 2024, 128, 4245−4257

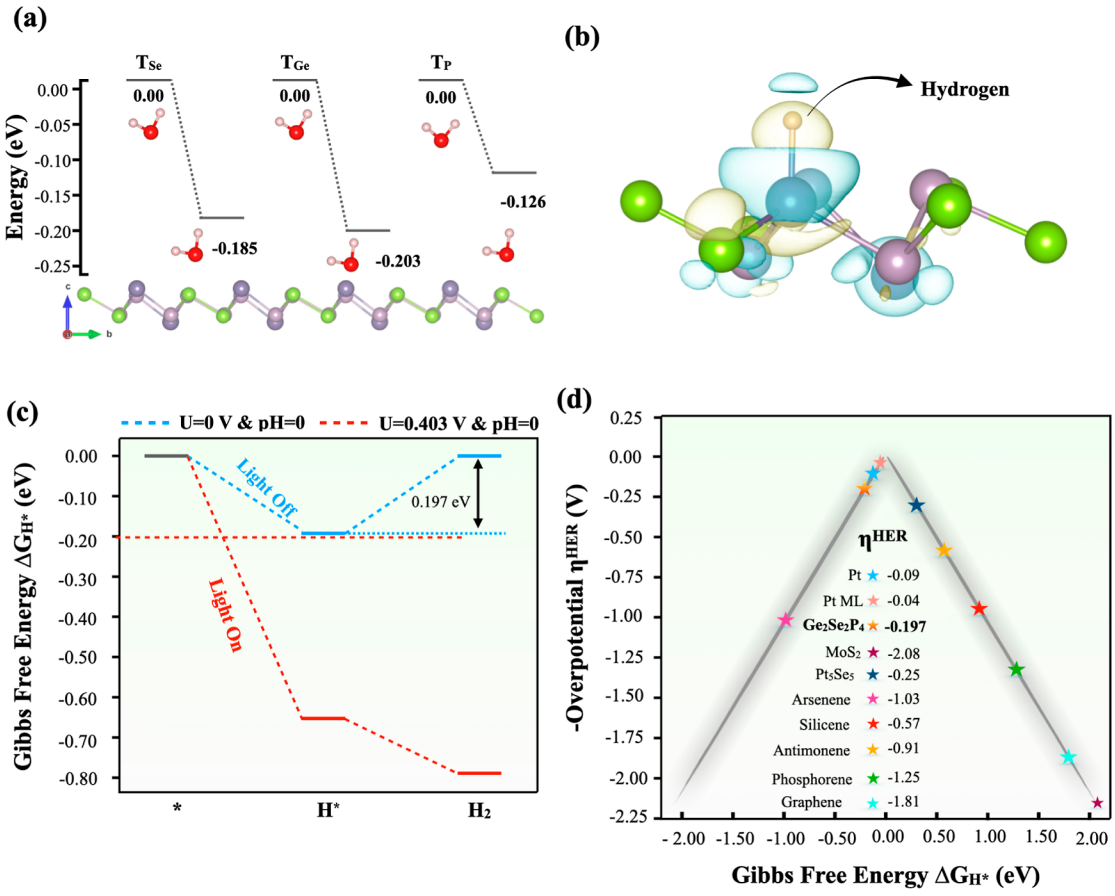

Figure 9. (a) Energy diagram of water molecules (H_2O) adsorbed at different active sites on the 2D $Ge_2Se_2P_4$ monolayer. (b) 3D charge density profile of the lowest energy configuration of hydrogen adsorption on $Ge_2Se_2P_4$. The charge accumulation/depletion area is indicated by the yellow/blue color, respectively. The isosurface value is set to be 0.15×10^{-3} eÅ^3. (c) Gibbs free energy diagram of HER at different conditions. (d) Free energy profile of HER mechanisms on the 2D $Ge_2Se_2P_4$ monolayer. (d) The HER volcano curve is being compared to other 2D materials that have been recently reported, including the widely used Pt.

$$H_2O(l) + O^* \rightarrow OOH^* + H^+ + e^- \quad (8)$$

$$OOH^* \rightarrow O_2(g) + H^+ + e^- \quad (9)$$

The theoretical Gibbs free energy difference (ΔG_{OH^*}, ΔG_{O^*}, and ΔG_{OOH^*}) of each step involving one e^- transfer is defined by the following equation

$$\Delta G = \Delta E + \Delta E_{ZPE} - T\Delta S + \Delta G_U - \Delta G_{pH} \quad (10)$$

where ΔE, ΔE_{ZPE}, and ΔS are the energy differences of adsorption, zero-point energy, and entropy between the adsorbed and freestanding states, respectively. The ΔE values were computed by DFT calculations, and ΔE_{ZPE} and ΔS were studied through DFT calculations and the standard thermodynamic data, as given in Table 2. ΔG_U ($\Delta G_U = -eU$) represents the extra potential bias supplied by an electron in the electrode, where U describes the potential difference with regard to the standard hydrogen electrode potential. ΔG_{pH} defines the effect of pH on the free energy ΔG, which is written by the formula $\Delta G_{pH} = -k_BT \times \ln[H^+] = k_BT \times \ln(10) \times pH$.

The variation of Gibbs free energy during $4e^-$ paths for OER could be defined as

$$\Delta G_1 = \Delta G_{OH^*} \quad (11)$$

$$\Delta G_2 = \Delta G_{O^*} - \Delta G_{OH^*} \quad (12)$$

$$\Delta G_3 = \Delta G_{OOH^*} - \Delta G_{O^*} \quad (13)$$

$$\Delta G_4 = 4.92 - \Delta G_{OOH^*} \quad (14)$$

The overpotential (η_{OER}) that could be employed to assess the catalytic performance of OER is derived from the subsequent equation

$$\eta_{OER} = \max\left\{\frac{\Delta G_1, \Delta G_2, \Delta G_3, \Delta G_4}{e}\right\} - 1.23 \quad (15)$$

In principle, achieving a full water-splitting operation requires that both photogenerated electrons and holes possess adequate energy to catalyze the HER and OER, respectively. Previous studies have established that the difference in energy levels between the E^{red}_{H+/H_2} and the VBM/CBM can serve as the external potential for photogenerated holes/electrons (U_h/U_e) to catalyze the HER/OER. It is noteworthy that the reduction potential and oxidation potential are given by the following equation

$$E^{red}_{H+/H_2} = -4.44 + pH \times 0.059 \quad (16)$$

$$E^{oxi}_{H_2/H_2O} = -5.67 + pH \times 0.059 \quad (17)$$

The external potential for photogenerated electrons and holes is given as follows

https://doi.org/10.1021/acs.jpcc.3c07237
J. Phys. Chem. C 2024, 128, 4245−4257

$$U_e = 0.40 - \mathrm{pH} \times 0.059 \quad (18)$$

$$U_h = 1.37 + \mathrm{pH} \times 0.059 \quad (19)$$

The computed reduction potential and oxidation potential show that the $Ge_2Se_2P_4$ monolayer is appropriate for overall water splitting for different values of pH ranging between 0 and 7. As a preliminary and crucial step, we first examined the adsorption of H_2O on the $Ge_2Se_2P_4$ monolayer to identify the most stable adsorption active site. To achieve this, we evaluated three starting adsorption sites. As shown in Figure 9a, the three considered sites exhibit negative adsorption energies. The P-site has the highest energy of −0.126 eV, followed by the Se-site with an adsorption energy of about −0.185 eV and the Ge-site at −0.203 eV, suggesting that the adsorption of H_2O on the $Ge_2Se_2P_4$ surface is energetically stable. It can also be noticed that the adsorbed water molecule is slightly deformed and that the deformed bond lengths between oxygen and hydrogen are about 0.973 and 0.977 Å from 0.963 Å and the H−O−H angle is about 103.425° from 104.0°. The adsorption energies in all three adsorption sites are higher compared to that of MoS_2.[82] Furthermore, by analyzing the charge transfer depicted in Figure 9b, it can be concluded that a substantial charge transfer takes place between $Ge_2Se_2P_4$ and the adsorbed water molecule, indicating that the adsorbed water molecule can be effectively activated by the activation site of $Ge_2Se_2P_4$ catalysts. Furthermore, the strong interactions between H_2O molecules and the $Ge_2Se_2P_4$ monolayer suggest that the photocatalytic activity is promising.

Hydrogen Evolution Reaction. Generally, the Gibbs free energy of the adsorbed intermediate hydrogen (ΔG_{H^*}) on the catalyst is typically used to evaluate the performance of the HER activity. An ideal catalyst should have a ΔG_{H^*} value of zero.[83,84] At first, we examined three distinct adsorption sites, namely, T_{Ge}, T_{Se}, and T_P, and H, and we selected the configuration with the most favorable energy. Originally, the H atom is positioned in the middle in the hexagonal lattice configuration. After full relaxation, the hydrogen atom undergoes a displacement toward the germanium atom, resulting in the formation of a bond between the hydrogen atom and two germanium atoms. The optimized structure of the $Ge_2Se_2P_4$ monolayer with a single hydrogen atom slightly changes the bond lengths near the site where the hydrogen is adsorbed. The distorted chemical bond lengths are calculated to be 2.437 Å from 2.486 Å for Ge−P and 2.316 Å from 2.620 Å for Ge−Se, and the Ge−H/P−H/Se−H bond lengths are found to be 1.545/1.435/1.479 Å, respectively. Generally, the criterion for determining whether a material exhibits HER activity is based on the standard rule of evaluating the $|\Delta G_{H^*}|$ value, which should be equal to or less than 0.2 eV.[85] As shown in Figure 9c,d and Table 2, the Gibbs free energy is about −0.197 eV when the $Ge_2Se_2P_4$ is in a dark environment (light off and $U = 0$). Additionally, it is observed that the process of HER can occur spontaneously when exposed to light since both ΔG_{H^*} steps are downward. For comparison, the HER activity performance of the $Ge_2Se_2P_4$ monolayer was found to be better than that of several other 2D materials, including MoS_2 (−2.08 eV), MoS_2−Mo edge (−0.36 eV), PtS_2 (0.86 eV), $PdTe_2$ (0.74 eV), $PtTe_2$ (0.54 eV), and $PtSe_2$ (0.63 eV).[86−89]

Table 2. Adsorption Energies (eV), Zero-Point Energy E_{ZPE} (eV), Entropy Contribution (eV), and the Gibbs Free Energy (eV) of Molecules and Adsorbates Used on the 2D $Ge_2Se_2P_4$ Monolayer

				HER		OER	
species	H_2(g)	H_2O(l)	O_2(g)	H*	OH*	O*	OOH*
ΔE				−0.42	2.67	0.78	3.06
E_{ZPE}	0.27	0.57	0.11	0.22	0.32	0.19	0.42
TS	0.40	0.67	0.63	0.01	0.15	0.01	0.22
ΔG	−6.76	−14.18	−8.84	−0.19	1.06	2.72	3.48

In addition, the charge transfer between $Ge_2Se_2P_4$ and the hydrogen atom was examined through Bader analysis.[90] Upon the hydrogen adsorption on the $Ge_2Se_2P_4$ surface, a charge transfer of about 0.33e from the surface to the H atom is obtained. Additionally, a distributed charge density at the most stable active site is computed as shown in Figure 9b, where yellow and blue colors indicate electron accumulation and charge depletion, respectively. Figure 9d illustrates a volcanic curve that compares the HER performance of $Ge_2Se_2P_4$ with previously reported 2D structures and well-examined Pt catalysts. The top values on the curve represent the highest catalytic activity. It is evident that the 2D $Ge_2Se_2P_4$ monolayer exhibits higher HER catalytic activity than that of other 2D materials. This indicates that optimizing the $Ge_2Se_2P_4$ monolayer with some other strategies, namely, single-atom catalysts, could further enhance its catalytic activity for HER.

Oxygen Evolution Reaction/Oxygen Reduction Reaction. Subsequently, a detailed investigation into the performance of OER and ORR activities was conducted on the 2D $Ge_2Se_2P_4$ monolayer. The OER reaction mechanism is intricate and comprises four elementary reaction pathways: (i) the initial dissociation of the water (H_2O) molecule into H^+ and OH* on the catalyst's surface; (ii) the further dissociation of HO* into H^+ and O*; (iii) the subsequent reaction of O* with the next H_2O molecule, resulting in H^+ and HOO*; and (iv) the final splitting of HOO* into H^+ and the O_2 molecule, followed by the release of O_2 from the catalyst's surface. The complete reaction mechanism for OER is illustrated in Figure 10a. Notably, each elementary step involves the simultaneous release of a cation (H^+) and an electron. Thus, in the OER mechanism, the release of a H^+ cation and an electron occurs concurrently at every reaction step. In this study, we have investigated the energetic stability of the OER mechanism on the 2D $Ge_2Se_2P_4$ monolayer by computing the lowest energy of all possible intermediates (O*, OH*, and HOO*). The corresponding Gibbs free energies for each reaction step have been determined and are presented in Figure 10b, and the overpotential (η_{OER}) for OER has been obtained based on the computed Gibbs free energy for each reaction step.

The rate-determining step for OER has been pinpointed by the dotted red line in Figure 10b at an electrode potential of U = 0 V and pH = 0 (light off). Our calculations show that the overpotential value for the 2D $Ge_2Se_2P_4$ monolayer is 0.42 V, and the transformation of OH* to O* is the rate-determining step. Notably, our calculated overpotential value (η_{OER}) for the $Ge_2Se_2P_4$ monolayer is lower than that of the extensively studied Pt(111) surface (0.76 V)[91] and slightly lower than those of the metal atom-supported 2D C2N monolayer (0.67 V)[92] and IrO_2 (0.56 V).[93] Moreover, we have computed the limiting potential step as illustrated by the dotted green line in Figure 10b at an electrode potential of U = 0 V and pH = 0, as well as in Figure 10c under light irradiation conditions. Our analysis shows that U_l^{OER} is 1.65 eV at pH = 0, which increases to 1.94 eV at pH = 7. Based on our findings, we suggest that

https://doi.org/10.1021/acs.jpcc.3c07237
J. Phys. Chem. C 2024, 128, 4245−4257

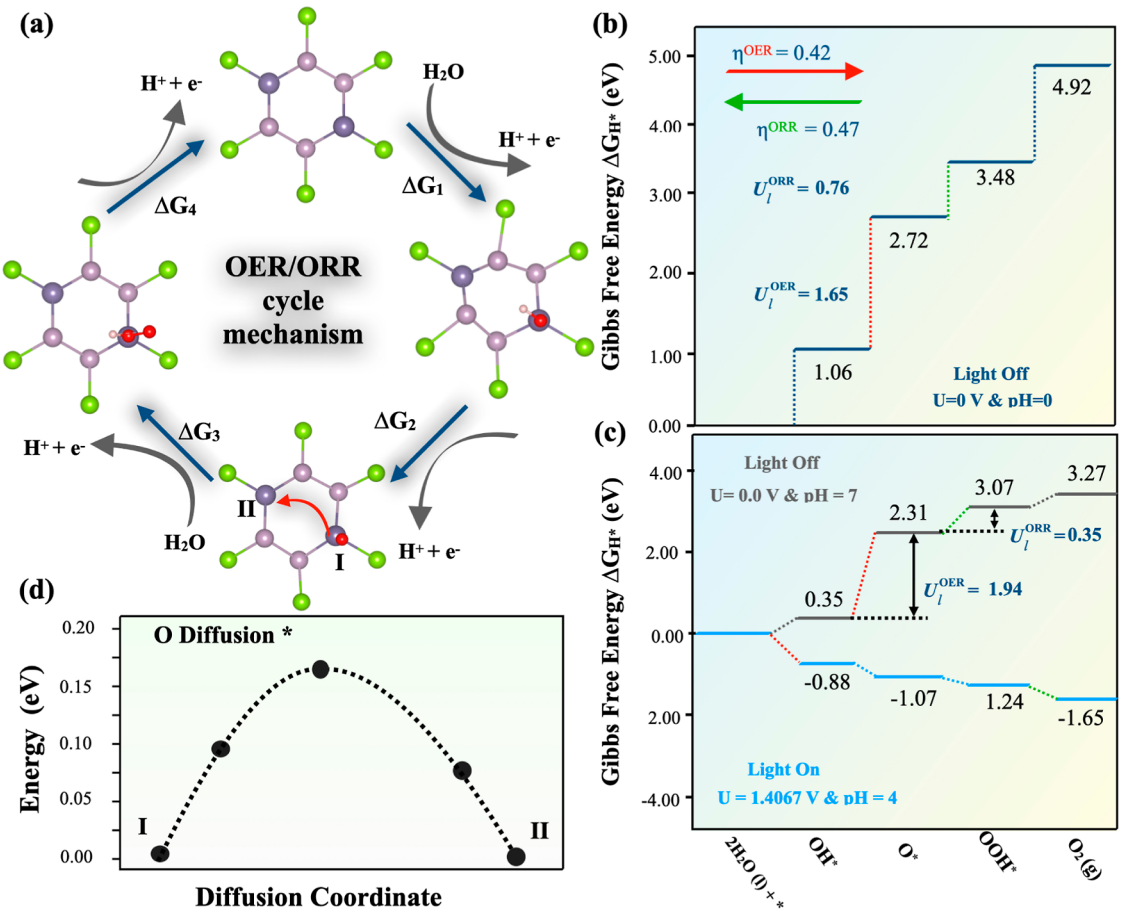

Figure 10. (a) The reaction pathway of the entire OER/ORR mechanism and its intermediates has been optimized to get the most efficient configuration for the dual-active site mechanisms. (b,c) Free energy diagram of OER/ORR mechanisms on 2D $Ge_2Se_2P_4$ at different conditions of U (V) and pH. The green/red dashed lines illustrate the rate-determining step for ORR/OER, respectively. (d) Activation energy barrier of O* from the catalytically active site I to II.

the 2D $Ge_2Se_2P_4$ monolayer has promising potential as an excellent choice for the OER mechanism catalyst.

Hence, we conducted a further analysis into distinct active adsorption sites and explored the migration behavior of O* intermediate at these sites (namely, site I and site II, as shown in Figure 10d). The inset within the red line demonstrates that the energy barrier for O* diffusion from site I to site II is 0.164 eV. The low activation energy and high stability of site II suggest that once O* is formed on the surface, it quickly moves to site II, which is the next elemental reaction leading to HOO* formation. These findings provide strong evidence supporting the feasibility of the dual active site mechanism. Furthermore, the transfer of O* from site I to site II in the OER process allows the vacant active site I to participate in the HER mechanism, generating H^+. Hence, site I also acts as an active site for the HER mechanism, further promoting the kinetic rate and overall efficiency of water splitting.

Moving on to the ORR mechanism, which involves the reduction of oxygen, we can complement our understanding of the OER mechanism. Using the four-elementary reaction mechanism, we calculate the overpotential for ORR (η_{ORR}) by determining the minimum step distance, which is the rate-determining step shown by the dotted green line in Figure 10b,c. The free energy diagram shows that each step of the ORR mechanism for each system shows a downward trend, which indicates that each reaction proceeds spontaneously. In a dark environment, the overpotential value is around 0.47 eV, and the limiting potential step is approximately 0.76 eV, which decreases to 0.35 eV at pH = 7. The computed overpotential value is slightly higher or equivalent to that of the well-defined catalyst Pt of 0.45 V,[91] suggesting that the 2D $Ge_2Se_2P_4$ monolayer is an excellent candidate for the ORR mechanism. These results indicate that the 2D $Ge_2Se_2P_4$ monolayer is a highly versatile photocatalyst, showing exceptional performance not only for the ORR but also for the HER and OER.

Solar to Hydrogen Efficiency. The solar to hydrogen (STH) conversion efficiency is determined by using the methodology suggested by Yang et al.[94] The STH efficiency may be defined as the product of the efficiencies of light absorption (noted as η_{abs}) and carrier utilization (denoted as η_{cu}) by the reaction process.

$$\eta_{STH} = \eta_{abs} \times \eta_{cu} \tag{20}$$

The light absorption efficiency is defined as

$$\eta_{abs} = \frac{\int_{E_g}^{\infty} P(h\omega)d(h\omega)}{\int_{0}^{\infty} P(h\omega)d(h\omega)} \tag{21}$$

where $P(h\omega)$ represents the AM1.5G solar energy flow at a specific photon energy $h\omega$ and E_g refers to the bandgap of the photocatalyst. The numerator indicates the light power density absorbed by the photocatalyst, while the denominator is the

https://doi.org/10.1021/acs.jpcc.3c07237
J. Phys. Chem. C 2024, 128, 4245−4257

Table 3. Summary of Various Photocatalytic Properties of the 2D $Ge_2Se_2P_4$ Monolayer, Including the Overpotential for HER ($\chi(H_2)$) and OER ($\chi(O_2)$), Photon Energy (E) at Different pH Levels, as Well as the Efficiency of Light Absorption (η_{abs}), Carrier Utilization (η_{cu}), and STH (η_{STH}) Energy Conversion

pH	$\chi(H_2)$	$\chi(O_2)$	E	η_{abs}	η_{cu}	η_{STH}	U_e	U_h
0	0.403	0.177	2.233	0.456	0.271	12.334	0.403	1.406
1	0.344	0.236	2.174	0.456	0.300	13.678	0.344	1.466
2	0.285	0.295	2.115	0.456	0.328	14.973	0.285	1.525
3	0.226	0.354	2.056	0.456	0.358	16.340	0.226	1.584
4	0.167	0.413	2.030	0.456	0.374	17.051	0.167	1.643
5	0.108	0.472	2.030	0.456	0.374	17.051	0.108	1.702
6	0.049	0.531	2.030	0.456	0.374	17.051	0.049	1.761
7	−0.009	0.589	2.030	0.456	0.374	17.051	−0.009	1.819

overall power density of the reference sunshine spectrum (AM1.5G). The efficiency of carrier utilization (η_{cu}) is defined as

$$\eta_{cu} = \frac{\Delta G_{H_2O} \int_E^{\infty} \frac{P(h\omega)}{h\omega} d(h\omega)}{\int_{E_g}^{\infty} P(h\omega) d(h\omega)} \tag{22}$$

where ΔG_{H_2O} denotes the Gibbs free energy change associated with the process of water splitting (1.23 eV) and the remainder of the numerator indicates the effective photocurrent density. E is the energy of photons that may be used in the water-splitting process.

$$E = \begin{cases} E_g, (\chi(H_2) \geq 0.2, \chi(O_2) \geq 0.6), \\ E_g + 0.2 - \chi(H_2), (\chi(H_2) < 0.2, \chi(O_2) \geq 0.6), \\ E_g + 0.6 - \chi(O_2), (\chi(H_2) \geq 0.2, \chi(O_2) < 0.6), \\ E_g + 0.8 - \chi(H_2) - \chi(O_2), (\chi(H_2) < 0.2, \chi(O_2) < 0.6). \end{cases} \tag{23}$$

To achieve a high efficiency, the STH efficiency of the $Ge_2Se_2P_4$ monolayer is determined as a function of the pH value. Table 3 shows the adjusted overpotentials $\chi(H_2)$ for HER and $\chi(O_2)$ for OER, the photon energy (E), the efficiency of light absorption η_{abc}, and carrier utilization η_{cu}. The values of η_{STH} rise from 12.334 to 17.051% from pH = 0 to pH = 4 and then stay constant as the pH value increases. Interestingly, the anticipated maximum value of η_{STH} (17.051%) for the $Ge_2Se_2P_4$ monolayer is higher than the previous report for GeN_3 (12.63%) and $AgBiP_2Se_6$ (10.3%) values, and it surpasses the crucial value of economic hydrogen generation through photocatalytic water splitting (10%).[72,95] As a result of these observations, the $Ge_2Se_2P_4$ monolayer has the potential to serve as an efficient photocatalyst for overall water splitting under moderately acidic conditions.

CONCLUSIONS

In summary, our investigation has revealed the potential of the novel 2D $Ge_2Se_2P_4$ monolayer as an exceptional candidate for photocatalytic applications. Through our computational analysis, we determined that the $Ge_2Se_2P_4$ monolayer behaves as a semiconductor, exhibiting a band gap of 1.81 eV based on the hybrid functional HSE06 approach, with the SOC effect showing minimal influence on its electronic properties. Notably, the $Ge_2Se_2P_4$ monolayer demonstrates directionally anisotropic carrier mobility, as the electron mobility in x-direction is 7×10^3 cm^2 V^{-1} s^{-1} surpassing the electron in y-direction which is 375.35 cm^2 V^{-1} s^{-1}. Our comprehensive study further unveils the superior catalytic performance of the $Ge_2Se_2P_4$ monolayer as HER/OER and OER/ORR bifunctional electrocatalysts. Its ability to operate with lower overpotentials suggests a highly efficient and versatile photocatalyst. These findings position the $Ge_2Se_2P_4$ monolayer as a promising candidate for advancing renewable energy production technologies. By shedding light on the remarkable properties of this material, our findings offer valuable insights into the development of cost-effective, high-performance photocatalysts, thereby driving the evolution of sustainable energy technologies.

AUTHOR INFORMATION

Corresponding Authors

Tuan V. Vu − *Laboratory for Computational Physics, Institute for Computational Science and Artificial Intelligence, Van Lang University, 70000 Ho Chi Minh City, Viet Nam; Faculty of Mechanical—Electrical and Computer Engineering, School of Technology, Van Lang University, 70000 Ho Chi Minh City, Viet Nam;* orcid.org/0000-0003-3872-8323; Email: tuan.vu@vlu.edu.vn

Poulumi Dey − *Department of Materials Science and Engineering, Faculty of Mechanical Engineering, Delft University of Technology, 2628 CD Delft, The Netherlands;* orcid.org/0000-0003-4679-1752; Email: p.dey@tudelft.nl

Nabil Khossossi − *Department of Materials Science and Engineering, Faculty of Mechanical Engineering, Delft University of Technology, 2628 CD Delft, The Netherlands;* orcid.org/0000-0002-3914-4162; Email: n.khossossi@tudelft.nl

Authors

Nguyen N. Hieu − *Institute of Research and Development, Duy Tan University, 550000 Da Nang, Vietnam; Faculty of Natural Sciences, Duy Tan University, 550000 Da Nang, Vietnam;* orcid.org/0000-0001-5721-960X

Dat D. Vo − *Laboratory for Computational Physics, Institute for Computational Science and Artificial Intelligence, Van Lang University, 70000 Ho Chi Minh City, Viet Nam; Faculty of Mechanical—Electrical and Computer Engineering, School of Technology, Van Lang University, 70000 Ho Chi Minh City, Viet Nam*

A. I. Kartamyshev − *Laboratory for Computational Physics, Institute for Computational Science and Artificial Intelligence, Van Lang University, 70000 Ho Chi Minh City, Viet Nam;*

https://doi.org/10.1021/acs.jpcc.3c07237
J. Phys. Chem. C 2024, 128, 4245−4257

Faculty of Mechanical—Electrical and Computer Engineering, School of Technology, Van Lang University, 70000 Ho Chi Minh City, Viet Nam

Hien D. Tong − *Faculty of Engineering, Vietnamese-German University, 820000 Binh Duong, Viet Nam*

Thuat T. Trinh − *Porelab, Department of Chemistry, Norwegian University of Science and Technology, 7491 Trondheim, Norway;* orcid.org/0000-0002-1721-6786

Vo Khuong Dien − *Department of Physics, National Cheng Kung University, 70101 Tainan, Taiwan;* orcid.org/0000-0002-7974-9852

Zakaryae Haman − *Laboratoire de Physique des Matèriaux et Modélisations des Systèmes, (LP2MS), Faculty of Sciences, Department of Physics, Moulay Ismail University, 50050 Meknes, Morocco*

Complete contact information is available at: https://pubs.acs.org/10.1021/acs.jpcc.3c07237

Notes

The authors declare no competing financial interest.

■ ACKNOWLEDGMENTS

This study was funded by the Nederlandse Organisatie voor Wetenschappelijk Onderzoek (The Netherlands Organization for Scientific Research, NWO) domain Science for the use of supercomputer facilities and the Norwegian University of Science and Technology. Thuat T. Trinh acknowledges funding from the Research Council of Norway (RCN), the Center of Excellence Funding Scheme, project no. 262644, PoreLab.

■ REFERENCES

(1) Rajalakshmi, N.; Balaji, R.; Ramakrishnan, S. *Sustainable Fuel Technologies Handbook*; Elsevier, 2021, pp 431−456.

(2) Ashraf, M.; Ullah, N.; Khan, I.; Tremel, W.; Ahmad, S.; Tahir, M. N. Photoreforming of Waste Polymers for Sustainable Hydrogen Fuel and Chemicals Feedstock: Waste to Energy. *Chem. Rev.* **2023**, *123*, 4443−4509.

(3) Maeda, K. K. J.; Domen, K. New Non-Oxide Photocatalysts Designed for Overall Water Splitting under Visible Light. *J. Phys. Chem. C* **2007**, *111*, 7851−7861.

(4) Concepcion, J. J.; Jurss, J. W.; Brennaman, M. K.; Hoertz, P. G.; Patrocinio, A. O. T.; Murakami Iha, N. Y.; Templeton, J. L.; Meyer, T. J. Making oxygen with ruthenium complexes. *Accounts Chem. Res.* **2009**, *42*, 1954−1965.

(5) Fajrina, N.; Tahir, M. A critical review in strategies to improve photocatalytic water splitting towards hydrogen production. *Int. J. Hydrogen Energy* **2019**, *44*, 540−577.

(6) Li, Y.; Li, Y.-L.; Sa, B.; Ahuja, R. Review of Two-Dimensional Materials for Photocatalytic Water Splitting from a Theoretical Perspective. *Catal. Sci. Technol.* **2017**, *7*, 545.

(7) Qiao, M.; Liu, J.; Wang, Y.; Li, Y.; Chen, Z. $PdSeO_3$ monolayer: promising inorganic 2D photocatalyst for direct overall water splitting without using sacrificial reagents and cocatalysts. *J. Am. Chem. Soc.* **2018**, *140*, 12256−12262.

(8) Su, T.; Shao, Q.; Qin, Z.; Guo, Z.; Wu, Z. Role of interfaces in two-dimensional photocatalyst for water splitting. *ACS Catal.* **2018**, *8*, 2253−2276.

(9) Sun, Y.; Sun, Z.; Gao, S.; Cheng, H.; Liu, Q.; Piao, J.; Yao, T.; Wu, C.; Hu, S.; Wei, S.; et al. Fabrication of flexible and freestanding zinc chalcogenide single layers. *Nat. Commun.* **2012**, *3*, 1057.

(10) Cao, S.; Low, J.; Yu, J.; Jaroniec, M. Polymeric photocatalysts based on graphitic carbon nitride. *Adv. Mater.* **2015**, *27*, 2150−2176.

(11) Yu, Y.; Yan, W.; Gao, W.; Li, P.; Wang, X.; Wu, S.; Song, W.; Ding, K. Aromatic ring substituted g-C_3N_4 for enhanced photocatalytic hydrogen evolution. *J. Mater. Chem. A* **2017**, *5*, 17199−17203.

(12) Mukherjee, M.; Jana, R.; Datta, A. Designing C_6N_6/C_2N van der Waals heterostructures for photogenerated charge carrier separation. *Phys. Chem. Chem. Phys.* **2021**, *23*, 3925−3933.

(13) Lv, X.; Wei, W.; Sun, Q.; Li, F.; Huang, B.; Dai, Y. Two-dimensional germanium monochalcogenides for photocatalytic water splitting with high carrier mobility. *Appl. Catal., B* **2017**, *217*, 275−284.

(14) Chowdhury, C.; Karmakar, S.; Datta, A. Monolayer group IV−VI monochalcogenides: low-dimensional materials for photocatalytic water splitting. *J. Phys. Chem. C* **2017**, *121*, 7615−7624.

(15) Rawat, A.; Jena, N.; Dimple, D.; De Sarkar, A. A comprehensive study on carrier mobility and artificial photosynthetic properties in group VI B transition metal dichalcogenide monolayers. *J. Mater. Chem. A* **2018**, *6*, 8693−8704.

(16) Liao, J.; Sa, B.; Zhou, J.; Ahuja, R.; Sun, Z. Design of high-efficiency visible-light photocatalysts for water splitting: MoS_2/AlN (GaN) heterostructures. *J. Phys. Chem. C* **2014**, *118*, 17594−17599.

(17) Zhuang, H. L.; Hennig, R. G. Single-layer group-III monochalcogenide photocatalysts for water splitting. *Chem. Mater.* **2013**, *25*, 3232−3238.

(18) Vu, T. V.; Phuc, H. V.; Kartamyshev, A. I.; Hieu, N. N. Enhanced out-of-plane piezoelectricity and carrier mobility in Janus γ-Sn_2XY (X/Y = S, Se, Te) monolayers: A first-principles prediction. *Appl. Phys. Lett.* **2023**, *122*, 061601.

(19) Vu, T. V.; Phuc, H. V.; Nguyen, C. V.; Vi, V. T. T.; Kartamyshev, A. I.; Hieu, N. N. Rashba-type spin splitting and transport properties of novel Janus $XWGeN_2$ (X = O, S, Se, Te) monolayers. *Phys. Chem. Chem. Phys.* **2022**, *24*, 16512−16521.

(20) Vu, T. V.; Anh, N. P.; Phuc, H. V.; Kartamyshev, A. I.; Hieu, N. N. Strong out-of-plane piezoelectricity and Rashba-type spin splitting in asymmetric structures: first-principles study for Janus γ-Sn_2OX (X = S, Se, Te) monolayers. *New J. Chem.* **2023**, *47*, 11660−11668.

(21) Jing, Y.; Ma, Y.; Li, Y.; Heine, T. GeP3: A small indirect band gap 2D crystal with high carrier mobility and strong interlayer quantum confinement. *Nano Lett.* **2017**, *17*, 1833−1838.

(22) Shojaei, F.; Kang, H. S. Partially planar BP_3 with high electron mobility as a phosphorene analog. *J. Mater. Chem. C* **2017**, *5*, 11267−11274.

(23) Ghosh, B.; Puri, S.; Agarwal, A.; Bhowmick, S. SnP_3: a previously unexplored two-dimensional material. *J. Phys. Chem. C* **2018**, *122*, 18185−18191.

(24) Feng, L.-P.; Li, A.; Wang, P.-C.; Liu, Z.-T. Novel two-dimensional semiconductor SnP_3 with high carrier mobility, good light absorption, and strong interlayer quantum confinement. *J. Phys. Chem. C* **2018**, *122*, 24359−24367.

(25) Miao, N.; Xu, B.; Bristowe, N. C.; Zhou, J.; Sun, Z. Tunable magnetism and extraordinary sunlight absorbance in indium triphosphide monolayer. *J. Am. Chem. Soc.* **2017**, *139*, 11125−11131.

(26) Lu, N.; Zhuo, Z.; Guo, H.; Wu, P.; Fa, W.; Wu, X.; Zeng, X. C. CaP_3: a new two-dimensional functional material with desirable band gap and ultrahigh carrier mobility. *J. Phys. Chem. Lett.* **2018**, *9*, 1728−1733.

(27) Olofsson, O.; Aava, U.; Haaland, A.; Resser, D.; Rasmussen, S.; Sunde, E.; Sørensen, N. A. X-Ray Investigations of the Tin-Phosphorus System. *Acta Chem. Scand.* **1970**, *24*, 1153−1162.

(28) Sun, S.; Meng, F.; Wang, H.; Wang, H.; Ni, Y. Novel two-dimensional semiconductor SnP_3: high stability, tunable bandgaps and high carrier mobility explored using first-principles calculations. *J. Mater. Chem. A* **2018**, *6*, 11890−11897.

(29) Zhu, X.-L.; Liu, P.-F.; Zhang, J.; Zhang, P.; Zhou, W.-X.; Xie, G.; Wang, B.-T. Monolayer SnP_3: An excellent p-type thermoelectric material. *Nanoscale* **2019**, *11*, 19923−19932.

(30) Yao, S.; Zhang, X.; Zhang, Z.; Chen, A.; Zhou, Z. 2D Triphosphides: SbP_3 and GaP_3 monolayer as promising photocatalysts for water splitting. *Int. J. Hydrogen Energy* **2019**, *44*, 5948−5954.

(31) Yuan, J.-H.; Cresti, A.; Xue, K.-H.; Song, Y.-Q.; Su, H.-L.; Li, L.-H.; Miao, N.-H.; Sun, Z.-M.; Wang, J.-F.; Miao, X.-S. TlP_5: an

unexplored direct band gap 2D semiconductor with ultra-high carrier mobility. *J. Mater. Chem. C* **2019**, *7*, 639−644.
(32) Andriotis, A. N.; Richter, E.; Menon, M. Prediction of a new graphenelike Si_2BN solid. *Phys. Rev. B* **2016**, *93*, 081413.
(33) Xie, Q.; Yuan, J.; Yu, N.; Wang, L.; Wang, J. Prediction of new group IV-V-VI monolayer semiconductors based on first principle calculation. *Comput. Mater. Sci.* **2017**, *135*, 160−164.
(34) Ding, Y.; Wang, Y. Tunable electronic and magnetic properties of graphene-like $XYBe_3$ (XY= BN, AlN, SiC, GeC) nanosheets with carrier doping: a first-principles study. *Phys. Chem. Chem. Phys.* **2018**, *20*, 6830−6837.
(35) Liu, Y.-L.; Jiang, X.-X.; Li, B.; Shi, Y.; Liu, D.-S.; Yang, C.-L. First principles study of photoelectrochemical water splitting in monolayer $Sn_2S_2P_4$ with high solar-to-hydrogen efficiency. *Appl. Phys. Lett.* **2021**, *119*, 143102.
(36) Zhu, Y.-L.; Yuan, J.-H.; Song, Y.-Q.; Xue, K.-H.; Wang, S.; Lian, C.; Li, Z.-N.; Xu, M.; Cheng, X.-M.; Miao, X.-S. Promising photocatalysts with high carrier mobility for water splitting in monolayer $Ge_2P_4S_2$ and $Ge_2As_4S_2$. *Int. J. Hydrogen Energy* **2019**, *44*, 21536−21545.
(37) Liu, H.-Y.; Yang, C.-L.; Wang, M.-S.; Ma, X.-G. Two-dimensional hexaphosphate $BiMP_6$ (M= Al, Ga, In) with desirable band gaps and ultrahigh carrier mobility for photocatalytic hydrogen evolution. *Appl. Surf. Sci.* **2020**, *517*, 146166.
(38) Elliott, R. J. Intensity of Optical Absorption by Excitons. *Phys. Rev.* **1957**, *108*, 1384−1389.
(39) Citrin, D. Radiative lifetimes of excitons in quantum wells: Localization and phase-coherence effects. *Phys. Rev. B: Condens. Matter Mater. Phys.* **1993**, *47*, 3832−3841.
(40) Xiao, J.; Zhao, M.; Wang, Y.; Zhang, X. Excitons in atomically thin 2D semiconductors and their applications. *Nanophotonics* **2017**, *6*, 1309−1328.
(41) Unuchek, D.; Ciarrocchi, A.; Avsar, A.; Watanabe, K.; Taniguchi, T.; Kis, A. Room-temperature electrical control of exciton flux in a van der Waals heterostructure. *Nature* **2018**, *560*, 340−344.
(42) Van der Donck, M.; Zarenia, M.; Peeters, F. Excitons and trions in monolayer transition metal dichalcogenides: A comparative study between the multiband model and the quadratic single-band model. *Phys. Rev. B* **2017**, *96*, 035131.
(43) Kresse, G.; Furthmüller, J. Efficient iterative schemes for ab initio total-energy calculations using a plane-wave basis set. *Phys. Rev. B: Condens. Matter Mater. Phys.* **1996**, *54*, 11169−11186.
(44) Kresse, G.; Furthmüller, J. Efficiency of ab-initio total energy calculations for metals and semiconductors using a plane-wave basis set. *Comput. Mater. Sci.* **1996**, *6*, 15−50.
(45) Blöchl, P. E.; Jepsen, O.; Andersen, O. K. Improved tetrahedron method for Brillouin-zone integrations. *Phys. Rev. B: Condens. Matter Mater. Phys.* **1994**, *49*, 16223−16233.
(46) Perdew, J. P.; Burke, K.; Ernzerhof, M. Generalized Gradient Approximation Made Simple. *Phys. Rev. Lett.* **1996**, *77*, 3865−3868.
(47) Heyd, J.; Scuseria, G. E.; Ernzerhof, M. Hybrid functionals based on a screened Coulomb potential. *J. Chem. Phys.* **2003**, *118*, 8207−8215.
(48) MacDonald, A. H.; Picket, W. E.; Koelling, D. D. A linearised relativistic augmented-plane-wave method utilising approximate pure spin basis functions. *J. Phys. C: Solid State Phys.* **1980**, *13*, 2675−2683.
(49) Luppi, E.; Weissker, H.-C.; Bottaro, S.; Sottile, F.; Veniard, V.; Reining, L.; Onida, G. Accuracy of the pseudopotential approximation in ab initio theoretical spectroscopies. *Phys. Rev. B: Condens. Matter Mater. Phys.* **2008**, *78*, 245124.
(50) Hybertsen, M. S.; Louie, S. G. First-Principles Theory of Quasiparticles: Calculation of Band Gaps in Semiconductors and Insulators. *Phys. Rev. Lett.* **1985**, *55*, 1418−1421.
(51) Ehrlich, S.; Moellmann, J.; Reckien, W.; Bredow, T.; Grimme, S. System-dependent dispersion coefficients for the DFT-D3 treatment of adsorption processes on ionic surfaces. *ChemPhysChem* **2011**, *12*, 3414−3420.
(52) Chaput, L.; Togo, A.; Tanaka, I.; Hug, G. Phonon-phonon interactions in transition metals. *Phys. Rev. B: Condens. Matter Mater. Phys.* **2011**, *84*, 094302.
(53) Sohier, T.; Calandra, M.; Mauri, F. Density functional perturbation theory for gated two-dimensional heterostructures: Theoretical developments and application to flexural phonons in graphene. *Phys. Rev. B* **2017**, *96*, 075448.
(54) Nosé, S. A unified formulation of the constant temperature molecular dynamics methods. *J. Chem. Phys.* **1984**, *81*, 511−519.
(55) Bardeen, J.; Shockley, W. Deformation potentials and mobilities in non-polar crystals. *Phys. Rev.* **1950**, *80*, 72−80.
(56) Cutkosky, R. Solutions of a Bethe-Salpeter equation. *Phys. Rev.* **1954**, *96*, 1135−1141.
(57) Fetter, A. L.; Walecka, J. D. *Quantum Theory of Many-Particle Systems*; Courier Corporation, 2012.
(58) Wu, H.-H.; Huang, H.; Zhong, J.; Yu, S.; Zhang, Q.; Zeng, X. C. Monolayer triphosphates MP_3 (M= Sn, Ge) with excellent basal catalytic activity for hydrogen evolution reaction. *Nanoscale* **2019**, *11*, 12210−12219.
(59) Ramasamy, P.; Kwak, D.; Lim, D.-H.; Ra, H.-S.; Lee, J.-S. Solution synthesis of GeS and GeSe nanosheets for high-sensitivity photodetectors. *J. Mater. Chem. C* **2016**, *4*, 479−485.
(60) Hu, Z.; Ding, Y.; Hu, X.; Zhou, W.; Yu, X.; Zhang, S. Recent progress in 2D group IV−IV monochalcogenides: synthesis, properties and applications. *Nanotechnology* **2019**, *30*, 252001.
(61) Kamal, C.; Chakrabarti, A.; Ezawa, M. Direct band gaps in group IV-VI monolayer materials: Binary counterparts of phosphorene. *Phys. Rev. B* **2016**, *93*, 125428.
(62) Cheng, Y. C.; Zhu, Z. Y.; Schwingenschlögl, U. Doped silicene: Evidence of a wide stability range. *Europhys. Lett.* **2011**, *95*, 17005.
(63) Cheng, Y. C.; Zhu, Z. Y.; Tahir, M.; Schwingenschlögl, U. Spin-orbit-induced spin splittings in polar transition metal dichalcogenide monolayers. *Europhys. Lett.* **2013**, *102*, 57001.
(64) Hung, N. T.; Nugraha, A. R. T.; Saito, R. Two-dimensional MoS_2 electromechanical actuators. *J. Phys. D: Appl. Phys.* **2018**, *51*, 075306.
(65) Mouhat, F.; Coudert, F. X. Necessary and sufficient elastic stability conditions in various crystal systems. *Phys. Rev. B: Condens. Matter Mater. Phys.* **2014**, *90*, 224104.
(66) Lee, C.; Wei, X.; Kysar, J. W.; Hone, J. Measurement of the elastic properties and intrinsic strength of monolayer graphene. *Science* **2008**, *321*, 385−388.
(67) Politano, A.; Chiarello, G. Probing the Young's modulus and Poisson's ratio in graphene/metal interfaces and graphite: a comparative study. *Nano Res.* **2015**, *8*, 1847−1856.
(68) Borlido, P.; Schmidt, J.; Huran, A. W.; Tran, F.; Marques, M. A.; Botti, S. Exchange-correlation functionals for band gaps of solids: benchmark, reparametrization and machine learning. *npj Comput. Mater.* **2020**, *6*, 96.
(69) Garza, A. J.; Scuseria, G. E. Predicting band gaps with hybrid density functionals. *J. Phys. Chem. Lett.* **2016**, *7*, 4165−4170.
(70) Fujishima, A.; Honda, K. Electrochemical photolysis of water at a semiconductor electrode. *Nature* **1972**, *238*, 37−38.
(71) Li, Y.; Li, Y.-L.; Sa, B.; Ahuja, R. Review of two-dimensional materials for photocatalytic water splitting from a theoretical perspective. *Catal. Sci. Technol.* **2017**, *7*, 545−559.
(72) Ju, L.; Shang, J.; Tang, X.; Kou, L. Tunable photocatalytic water splitting by the ferroelectric switch in a 2D $AgBiP_2Se_6$ monolayer. *J. Am. Chem. Soc.* **2020**, *142*, 1492−1500.
(73) Kudo, A.; Miseki, Y. Heterogeneous photocatalyst materials for water splitting. *Chem. Soc. Rev.* **2009**, *38*, 253−278.
(74) Phoon, B. L.; Lai, C. W.; Juan, J. C.; Show, P.-L.; Pan, G.-T. Recent developments of strontium titanate for photocatalytic water splitting application. *Int. J. Hydrogen Energy* **2019**, *44*, 14316−14340.
(75) Khuong Dien, V.; Li, W.-B.; Lin, K.-I.; Thi Han, N.; Lin, M.-F. Electronic and optical properties of graphene, silicene, germanene, and their semi-hydrogenated systems. *RSC Adv.* **2022**, *12*, 34851−34865.

https://doi.org/10.1021/acs.jpcc.3c07237
J. Phys. Chem. C 2024, 128, 4245−4257

(76) Fox, M. *Optical Properties of Solids*, 2nd ed.; Oxford University Press, 2010.
(77) Penn, D. R. Wave-number-dependent dielectric function of semiconductors. *Phys. Rev.* **1962**, *128*, 2093−2097.
(78) Qiu, D. Y.; Da Jornada, F. H.; Louie, S. G. Optical spectrum of MoS_2: many-body effects and diversity of exciton states. *Phys. Rev. Lett.* **2013**, *111*, 216805.
(79) Zhu, B.; Chen, X.; Cui, X. Exciton binding energy of monolayer WS_2. *Sci. Rep.* **2015**, *5*, 9218.
(80) Qiao, J.; Kong, X.; Hu, Z.; Yang, F.; Ji, W. Few layered black Phosphorus: emerging 2D semiconductor with high anisotropic carrier mobility and linear dichroism. *Nat. Commun.* **2014**, *5*, 4475.
(81) Atkins, P.; De Paula, J.; Friedman, R. *Physical Chemistry: Quanta, Matter, and Change*; Oxford University Press: USA, 2013.
(82) Ma, X.; Wu, X.; Wang, H.; Wang, Y. A Janus MoSSe monolayer: a potential wide solar-spectrum water-splitting photocatalyst with a low carrier recombination rate. *J. Mater. Chem. A* **2018**, *6*, 2295−2301.
(83) Singh, D.; Khossossi, N.; Ainane, A.; Ahuja, R. Modulation of 2D GaS/BTe vdW heterostructure as an efficient HER catalyst under external electric field influence. *Catal. Today* **2021**, *370*, 14−25.
(84) Singh, D.; Khossossi, N.; Luo, W.; Ainane, A.; Ahuja, R. 2D Janus and non-Janus diamanes with an in-plane negative Poisson's ratio for energy applications. *Mater. Today Adv.* **2022**, *14*, 100225.
(85) Huang, B.; Zhou, N.; Chen, X.; Ong, W.-J.; Li, N. Insights into the electrocatalytic hydrogen evolution reaction mechanism on two-dimensional transition-metal carbonitrides (MXene). *Chem.—Eur. J.* **2018**, *24*, 18479−18486.
(86) Huang, X.; Leng, M.; Xiao, W.; Li, M.; Ding, J.; Tan, T. L.; Lee, W. S. V.; Xue, J. Activating basal planes and S-terminated edges of MoS_2 toward more efficient hydrogen evolution. *Adv. Funct. Mater.* **2017**, *27*, 1604943.
(87) Tsai, C.; Abild-Pedersen, F.; Nørskov, J. K. Tuning the MoS_2 edge-site activity for hydrogen evolution via support interactions. *Nano Lett.* **2014**, *14*, 1381−1387.
(88) Chia, X.; Adriano, A.; Lazar, P.; Sofer, Z.; Luxa, J.; Pumera, M. Layered platinum dichalcogenides (PtS_2, $PtSe_2$, and $PtTe_2$) electrocatalysis: monotonic dependence on the chalcogen size. *Adv. Funct. Mater.* **2016**, *26*, 4306−4318.
(89) Chia, X.; Sofer, Z.; Luxa, J.; Pumera, M. Layered noble metal dichalcogenides: tailoring electrochemical and catalytic properties. *ACS Appl. Mater. Interfaces* **2017**, *9*, 25587−25599.
(90) Sanville, E.; Kenny, S. D.; Smith, R.; Henkelman, G. Improved grid-based algorithm for Bader charge allocation. *J. Comput. Chem.* **2007**, *28*, 899−908.
(91) Keith, J. A.; Jerkiewicz, G.; Jacob, T. Theoretical investigations of the oxygen reduction reaction on Pt (111). *ChemPhysChem* **2010**, *11*, 2779−2794.
(92) Zhang, X.; Chen, A.; Zhang, Z.; Jiao, M.; Zhou, Z. Transition metal anchored C_2N monolayers as efficient bifunctional electrocatalysts for hydrogen and oxygen evolution reactions. *J. Mater. Chem. A* **2018**, *6*, 11446−11452.
(93) Man, I. C.; Su, H.-Y.; Calle-Vallejo, F.; Hansen, H. A.; Martínez, J. I.; Inoglu, N. G.; Kitchin, J.; Jaramillo, T. F.; Nørskov, J. K.; Rossmeisl, J. Universality in oxygen evolution electrocatalysis on oxide surfaces. *ChemCatChem* **2011**, *3*, 1159−1165.
(94) Fu, C.-F.; Sun, J.; Luo, Q.; Li, X.; Hu, W.; Yang, J. Intrinsic electric fields in two-dimensional materials boost the solar-to-hydrogen efficiency for photocatalytic water splitting. *Nano Lett.* **2018**, *18*, 6312−6317.
(95) Li, H.; Jiang, X.; Xu, X.; Xu, G.; Li, D.; Li, C.; Cui, B.; Liu, D.-S. High mobility and enhanced photoelectric performance of two-dimensional ternary compounds NaCuX (X= S, Se, and Te). *Phys. Chem. Chem. Phys.* **2021**, *23*, 2475−2482.

https://doi.org/10.1021/acs.jpcc.3c07237
J. Phys. Chem. C 2024, 128, 4245−4257